WILEY | Hindawi

Research Article

Pathloss Modeling and Analysis for Intelligent Reflecting Surface-Assisted Terahertz MIMO Wireless Systems

Yuqing Yang,[1] Weimin Wang [ID],[1] Yongle Wu,[2] Bihua Tang,[1] and Yuanan Liu[1]

[1]*School of Electronic Engineering, Beijing University of Posts and Telecommunications, Beijing, China*
[2]*School of Integrated Circuits, Beijing University of Posts and Telecommunications, Beijing, China*

Correspondence should be addressed to Weimin Wang; wangwm@bupt.edu.cn

In this paper, the impact of the intelligent reflecting surface (IRS) on the propagation characteristics is analyzed from the arguments of the physical and electromagnetic characteristics of the channel. Analytical expressions for free-space pathloss are derived based on the terahertz multiple-input multiple-output (MIMO) channel model in different communication scenarios. This calculation method is broadly applicable and is used to characterize pathloss as a function of the configuration of our system model. Numerical results show that setting the phase matrix of IRS based only on the angle of arrival (AoA) and angle of departure (AoD) can significantly reduce the pathloss when the far-field condition is met. However, when the distance between the transceiver and the IRS is the same order of magnitude or less than the side length of the IRS, both direction and distance information are required to configure the IRS. This model provides an insightful consideration in the design of IRS-assisted wireless system.

1. Introduction

To meet the requirement of ultrawideband communication for over 100 billion user equipment in the forthcoming sixth-generation (6G) network, higher frequency communication and a variety of wireless technologies have been proposed [1]. Control of the propagation channel is a promising method to break the channel capacity boundary in the future [2]. Enhancing the complexity of physical layer technology is a commonly employed strategy to achieve higher data rates [3]. As an emerging technology, the IRS changes the channel characteristics during propagation directly, improving the efficiency and bandwidth of the communication system.

The IRS consists of a large number of low-cost passive components that can be artificially designed and programmed to change the phase of the received signal. By changing the phase matrix, beamforming and interference suppression at specific receivers can be realized [4, 5]. There-fore, the IRS technology has generated great interest of academia and industry, the RIS TECH Alliance (RISTA) was formed in April 2022, and the RIS-related discussions are also underway in the 3rd Generation Partnership Project (3GPP) Rel-18 [6].

Many important aspects of IRS-assisted wireless communication systems are investigated, including electromagnetic characteristics [7], channel estimation [8], modeling [9], and joint precoding [10]. However, there is only a limited number of papers that consider the design and analysis of IRS-assisted communication in the terahertz (THz) band [11]. The strong atmosphere molecule absorption attenuation and penetration loss during propagation make the implementation of the IRS necessary.

The realistic and pervasive three-dimensional (3D) system model is crucial for the analysis of IRS [12]. However, the standardized channel model has not been developed presently, and many proposed models are specific to limited communication scenarios.
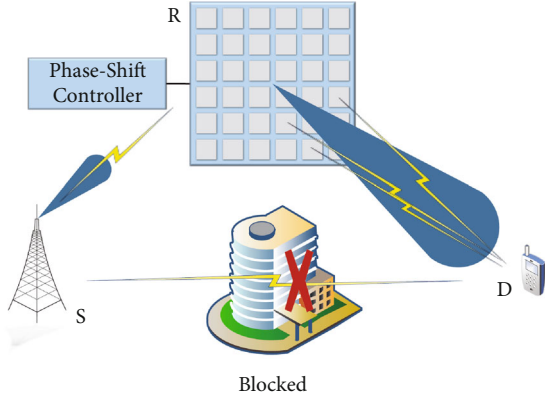
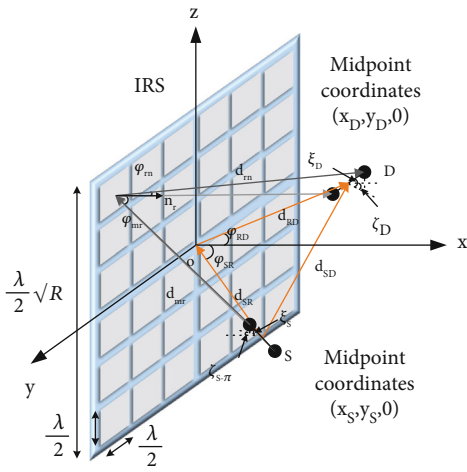FIGURE 1: Model of IRS-assisted wireless communication system.

FIGURE 2: Schematic diagram of IRS-assisted MIMO wireless communication system.

TABLE 1: List of main symbols.

Symbol	Description
R	Number of unit cells on the IRS
$\kappa(f)$	The molecular absorption coefficient
d_{mr}	Distance between the transmitting antenna unit M and the rth unit on the IRS
ξ_S/ξ_D	The elevation angle of the antenna array of the source/destination
φ_{SR}	Azimuth AoA on the IRS
φ_{mr}	Angle between the transmitting wave and the normal of the rth unit on the IRS
δ_S/δ_D	Distance between the antenna units at the source/destination
ε_r	The efficiency of the unit cells and the insertion loss associated with the generation of the phase shift
d_{rn}	Distance between the rth unit on the IRS and the receiving antenna unit N
ζ_S/ζ_D	The azimuth angle of the antenna array of the source/destination
φ_{RD}	Azimuth DoA on the IRS
φ_{rn}	Angle between the reflected wave and the normal of the rth unit on the IRS
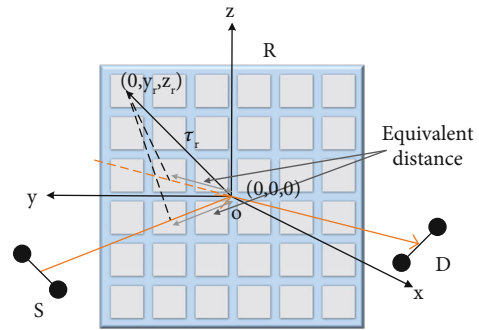
FIGURE 3: The proposed PiBS communication scenario.

TABLE 2: Simulation parameters.

Parameter	Value
Frequency	$f = 100\,\text{GHz}$
The number of antenna element in the S and D	$M = N = 2$
Azimuth and elevation angle of the antenna units in the S	$\xi_S = \pi/3,\ \zeta_S = 13\pi/12$
Azimuth and elevation angle of the antenna units in the D	$\xi_D = \pi/4,\ \zeta_D = \pi/6$
The interval of S/D antenna units	$\delta_S = \delta_D = \dfrac{\lambda}{2}$
Transmitting power	$P_t = 10\,\text{dBm}$

To the best of the authors' knowledge, the study of IRS-assisted MIMO communication system models in THz band is still in its infancy [13–19]. In [13], the latest research on reconfigurable intelligent surface- (RIS-) assisted wireless networks is summarized and the differences between the principles of RIS technology and similar technologies are analyzed. In [14], a channel model for double-IRS-assisted unmanned aerial vehicle (UAV) communication operated at sub-6G band is proposed. In [15], two power allocation methods that can achieve energy savings are proposed, one using the gradient descent method to calculate the phase coefficient of RIS before power allocation and the other using sequential fractional planning to optimize the phase shift, and it is found that RIS-based power allocation can improve the energy efficiency by three times compared to using conventional amplify-and-forward (AF) relaying. In addition, since decode-and-forward (DF) relaying outperforms AF relaying, the papers [16, 17] further compare the performance of DF relaying with IRS. In [18], although it analyzed in detail the coverage enhancement of cellular networks with the assistance of RIS, it mainly focused on the millimeter wave band and did not further consider the terahertz range. In [19], the IRS-assisted free-space pathloss model for wireless communication was established for several scenarios and actual measurement data
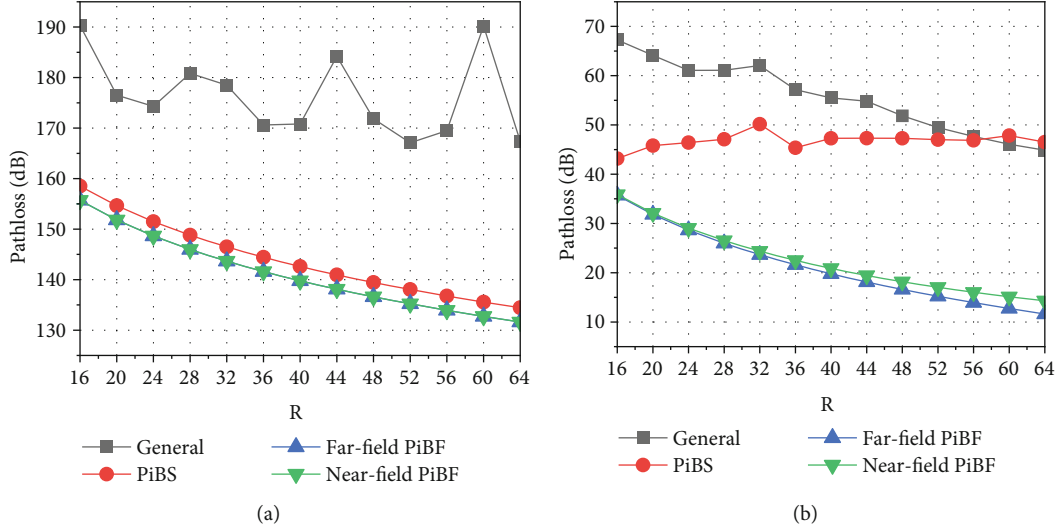
FIGURE 4: Simulation results of the variation of pathloss with the size of the IRS: (a) the far-field case; (b) the near-field case.

were provided for verification, but the paper only studied the single-input single-output (SISO) case at 10 GHz.

Against this background, the main contributions of this paper are listed as follows: (1) consider the MIMO transmission framework to improve the single channel transceiver antenna gain to solve the problem of large attenuation of terahertz signal atmospheric molecular absorption and establish a model for the application of IRS in the MIMO channel and (2) the IRS-assisted wireless communication channel model is introduced from the perspective of electromagnetic theory. A generalized free-space pathloss (FSPL) model is derived, and the specific forms of the pathloss in three practical scenarios are further deduced. The effect of the distance between the transceiver and the IRS, the transmission direction, and the IRS size on the FSPL is elucidated.

The following sections of the paper are organized as follows: Section 2 presents the system model, and the general problem formulation is given. Section 3 presents the analytical expressions for the pathloss of the model in different scenarios. The numerical results are analyzed and discussed in Section 4. Finally, conclusions are given in Section 5.

Notations: the bold letters denote matrices and vectors. The superscript $(\cdot)^{\mathrm{H}}$ is the Hermitian transpose, the expectation is $\mathbf{E}\{\cdot\}$, and $\mathbb{CN}(\cdot)$ is the complex Gaussian distribution. A diagonal matrix is diag (x) with $\mathbf{x}$ in the diagonal. Finally, $\mathbf{E}_{MN}$ is the $M \times N$ identity matrix.

2. System Model

In the 3D system model we proposed, the base station (BS) is represented by S and the user equipment (UE) is represented by D, as shown in Figure 1. When the line-of-sight (LoS) path is obscured by obstacles such as buildings, we assume that the LoS path does not exist due to the strong directivity of the THz wave.

As shown in Figure 2, the S with M antennas transmit the signal to the D with N antennas. The IRS is located in the y-z plane in a Cartesian coordinate system, and the geometric center of the IRS is located at the origin of the coordinate system. The IRS consists of $\sqrt{R} \times \sqrt{R}$ phase-shifted units, and the side length of each unit is $\lambda/2$. The main symbols in the model and their description are shown in Table 1.

In particular, d_{SR}, d_{RD}, and d_{SD} are used to denote the Euclidean distances of BS-IRS, IRS-UE, and BS-UE. $\mathbf{h}_{\mathrm{SR}}$, $\mathbf{h}_{\mathrm{RD}}$, and $\mathbf{H}_{\mathrm{SD}}$ stand for the complex CIR of the BS-IRS, IRS-UE, and BS-UE, respectively. $\boldsymbol{\tau}_m = (\delta_{\mathrm{S}}/2) \bullet (\cos \xi_m \cos \zeta_m, \cos \xi_m \sin \zeta_m, \sin \xi_m), m \epsilon \{1, 2\}$ is the vector expression of the antenna unit at the source; $\boldsymbol{\tau}_n = (\delta_{\mathrm{D}}/2) \bullet (\cos \xi_n \cos \zeta_n, \cos \xi_n \sin \zeta_n, \sin \xi_n), n \epsilon \{1, 2\}$ is the vector expression of the antenna unit at the destination. $\tilde{\mathbf{d}}_{\mathrm{SR}} = (-\cos\varphi_{\mathrm{SR}}, -\sin\varphi_{\mathrm{SR}}, 0)$ is the unit direction vector of the distance d_{SR}; $\tilde{\mathbf{d}}_{\mathrm{RD}} = (\cos\varphi_{\mathrm{RD}}, -\sin\varphi_{\mathrm{RD}}, 0)$ is the unit direction vector of the distance d_{RD}.

The phase shift matrix introduced by the IRS is denoted as $\boldsymbol{\Theta} = \mathrm{diag}\,(\exp\,(j\theta_1), \cdots, \exp\,(j\theta_R))$, where $\theta_r \in [-\pi, \pi], \forall r$. The signal $\mathbf{s}$ is transmitted from the S and satisfies $\mathbf{E}\{|\mathbf{s}|^2\} = 1$. Therefore, the signal received by D can be expressed as

$$\mathbf{y} = \sqrt{P_{\mathrm{t}}}\left(\mathbf{H}_{\mathrm{SD}} + \mathbf{h}_{\mathrm{SR}}^{\mathrm{H}} \Theta \mathbf{h}_{\mathrm{RD}}\right)\mathbf{s} + \mathbf{n}, \qquad (1)$$

where P_{t} is the transmit power, $\mathbf{n}$ is the additive white Gaussian noise, and $\mathbf{n} \sim \mathbb{CN}(0, \sigma^2 \mathbf{E}_{MN})$.

3. The Pathloss Model

It is assumed that the polarization of the transceiver is always matched in the transmission process. According to the Friis formula, the received signal power of IRS-assisted
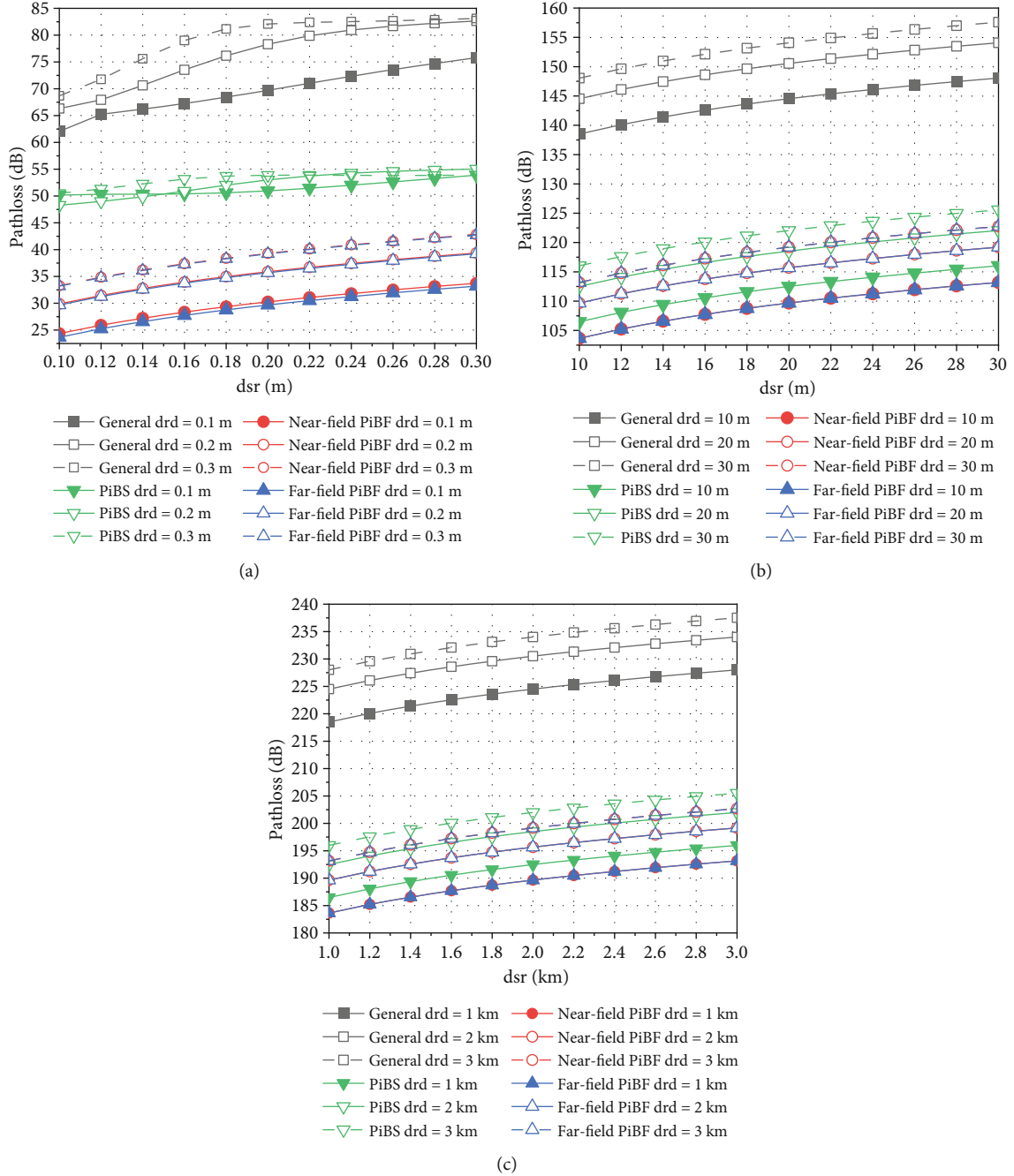
FIGURE 5: Simulation results for the variation of pathloss with the distance between the source/destination and the IRS: (a) far field; (b) threshold of the near and far fields; (c) near field.

wireless communication is as follows:

$$
\begin{aligned}
P_R = &\left(\frac{\lambda}{4\pi}\right)^4 P_T G_T G_R \\
&\cdot \left| \sum_{m=1}^{M} \sum_{n=1}^{N} \sum_{r=1}^{R} b_{r,mn} \sqrt{\frac{G_t(\varphi_m) G_e(\varphi_{mr}) G_e(\varphi_{rn}) G_r(\varphi_n)}{d_{mr}^2 d_{rn}^2}} e^{j\gamma_{r,mn}} \right|^2 \varepsilon_r \sigma_f .
\end{aligned}
$$

$$(2)$$

Proof. The proof is provided in the appendix.   □

In formula (2), $G_e(\varphi)$, $G_t(\varphi)$, and $G_r(\varphi)$ denote the radiation pattern of the IRS, the antenna of S, and the antenna of D, respectively. φ_m and φ_n denote the angle between the transmitting and receiving antenna unit and the peak of the radiation pattern of the BS. $\gamma_{r,mn} = (2\pi/\lambda) \bullet (d_{mr} + d_{rn})$ indicates the phase shift generated during the propagation. $\sigma_f = \exp(-\kappa(f) \bullet (d_{mr} + d_{rn}))$ denotes the terahertz wave absorption loss coefficient, and $\kappa(f)$ is obtained from [20]. $b_{r,mn} = e^{j\theta_r}$ is relative to the specific communication scenario, and θ_r is phase of the rth unit cell configured by the IRS.
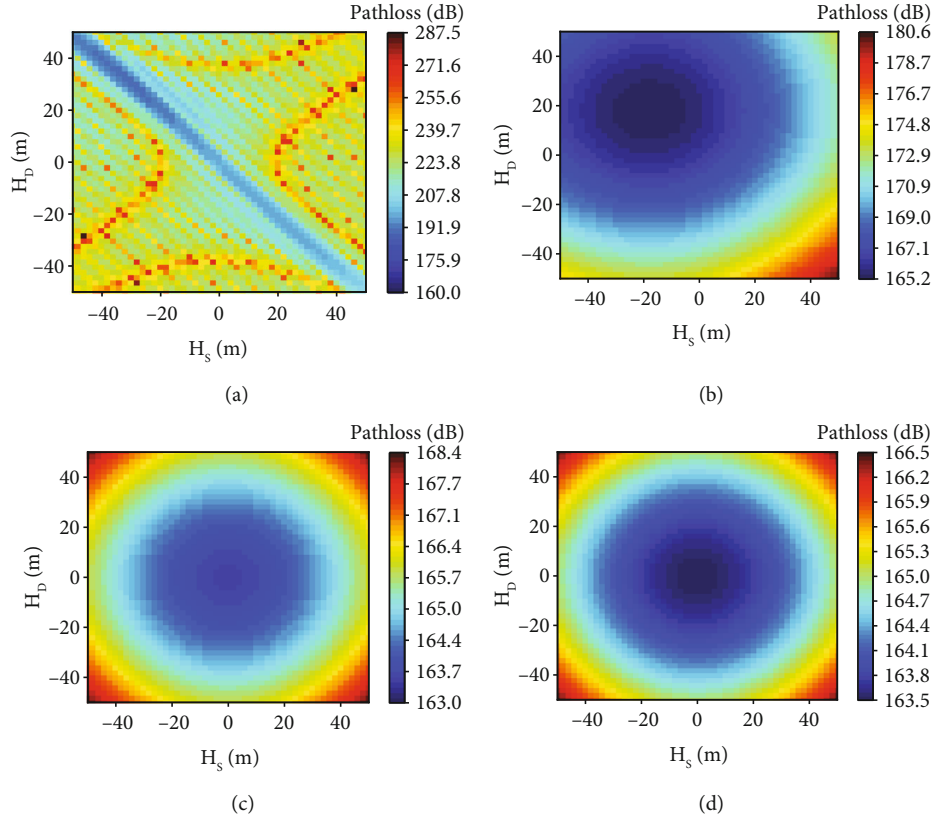
(a)

(b)

(c)

(d)

FIGURE 6: Simulation results for the variation of pathloss with the vertical distance of the S and D: (a) the general scenario; (b) the PiBS scenario; (c) the near-field PiBF scenario; (d) the far-field PiBF scenario.

Formula (2) indicates that the transceiver is interchangeable, which has important implications for the uplink and downlink design. According to formula (2), the pathloss can be obtained as

$$PL = \left(\left(\frac{\lambda}{4\pi} \right)^4 \cdot \left| \sum_{m=1}^{M} \sum_{n=1}^{N} \sum_{r=1}^{R} b_{r,mn} \sqrt{\frac{G_t(\varphi_m) G_e(\varphi_{mr}) G_e(\varphi_{rn}) G_r(\varphi_n)}{d_{mr}^2 d_{rn}^2}} e^{j\gamma_{r,mn}} \right|^2 \varepsilon_r \sigma_f \right)^{-1},$$

(3)

where due to the strong directionality of the terahertz antenna, we use the normalized power radiation model expressed as formula (4) [21] to represent the radiation pattern of the transceiver antenna and the reflection units of the IRS.

$$G(\varphi) = \begin{cases} \cos^3(\varphi), 0 \le \varphi \le \frac{\pi}{2}, \\ 0, \frac{\pi}{2} \le \varphi \le \pi. \end{cases}$$

(4)

The directions of peak value in radiation pattern of the transmitting antenna and the receiving antenna are both pointing at the geometric center of the IRS. In the model we proposed, we assume that the phase shift is continuous. Therefore, the phase configuration of the IRS is separated into the following three scenarios.

3.1. General Scenario.
In the general scenario, the phase shift $\theta_r = 0, r\epsilon\{1, 2, \cdots, R\}$. Therefore, $b_{r,mn} = 1$. The pathloss can be written as

$$PL = \left(\left(\frac{\lambda}{4\pi} \right)^4 \cdot \left| \sum_{m=1}^{M} \sum_{n=1}^{N} \sum_{r=1}^{R} \sqrt{\frac{G_t(\varphi_m) G_e(\varphi_{mr}) G_e(\varphi_{rn}) G_r(\varphi_n)}{d_{mr}^2 d_{rn}^2}} e^{j\gamma_{r,mn}} \right|^2 \varepsilon_r \sigma_f \right)^{-1}.$$

(5)

3.2. Far-Field and Near-Field PiBF Scenarios.
In the PiBF scenario, we take the exact value of $\gamma_{r,mn}$ which relate to m, n, and r. To obtain the minimum pathloss, the phase shift of the rth unit cell is $\theta_r = -\gamma_{r,mn}$. Therefore, $b_{r,mn} = \exp(-j\gamma_{r,mn})$.

When the distance among the transceiver and the IRS meets the far-field condition which means the $d_{SR} > 2D^2/\lambda$ and $d_{RD} > 2D^2/\lambda$, the distance difference among the transceiver and different unit cells on the IRS can be ignored. $\gamma_{r,mn}$ relates to m and n. Therefore, the pathloss can be written as

$$PL = \left(\left(\frac{\lambda}{4\pi} \right)^4 \cdot M^2 N^2 R^2 \frac{G_t(\varphi_m) G_e(\varphi_{SR}) G_e(\varphi_{RD}) G_r(\varphi_n)}{d_{SR}^2 d_{RD}^2} \varepsilon_r \sigma_f \right)^{-1}.$$
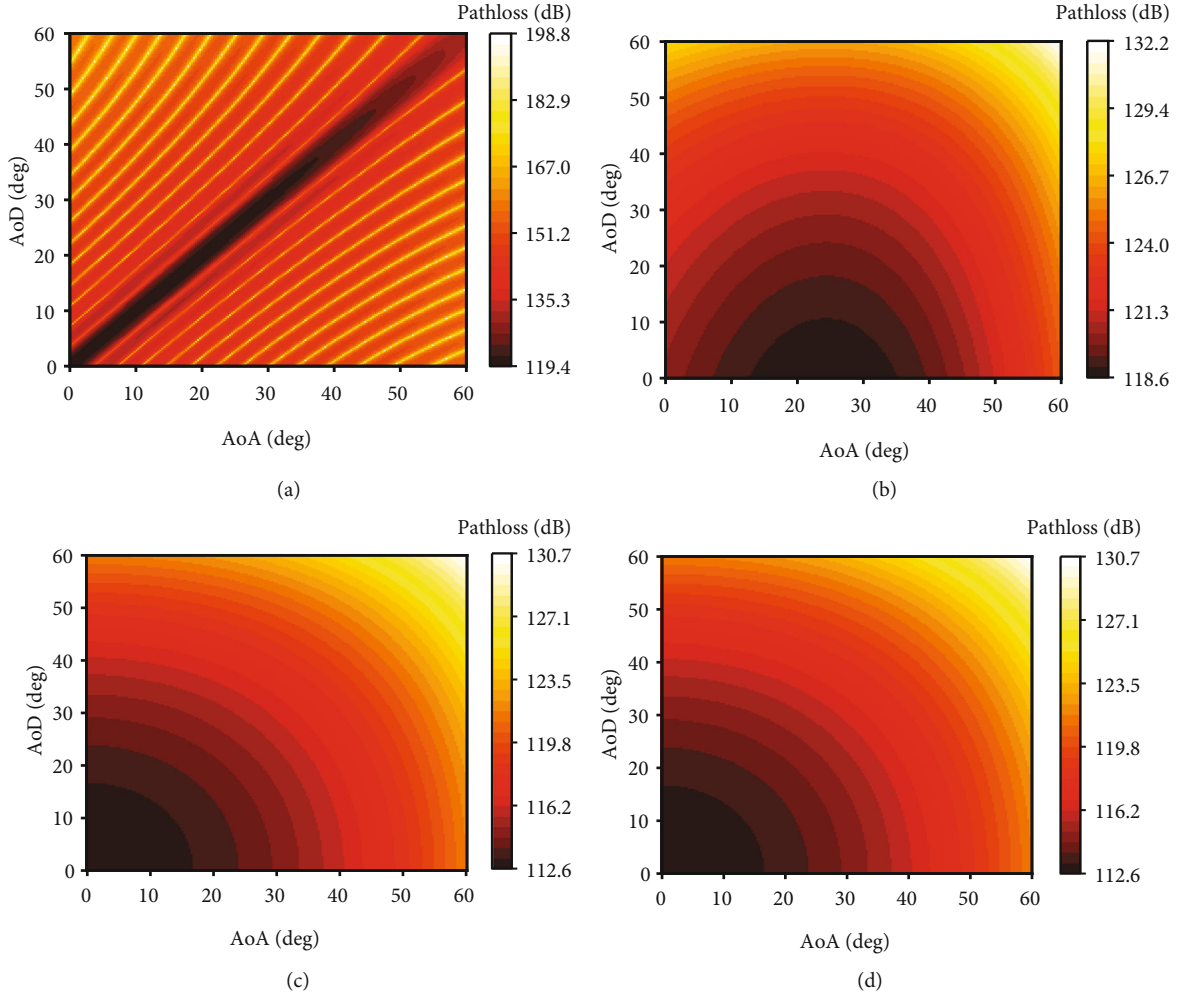
(6)

(a)

(b)

(c)

(d)

FIGURE 7: Simulation results of the variation of pathloss with the angle between source and destination and y-axis for different modes: (a) the general scenario; (b) the PiBS scenario; (c) the near-field PiBF scenario; (d) the far-field PiBF scenario.

The distance only meets requirement of near field, including (1) $d_{SR} > 2D^2/\lambda$ and $d_{RD} < 2D^2/\lambda$, (2) $d_{SR} < 2D^2/\lambda$ and $d_{RD} > 2D^2/\lambda$, and (3) $d_{SR} < 2D^2/\lambda$ and $d_{RD} < 2D^2/\lambda$. $\gamma_{r,mn}$ relates to r, m, and n. The pathloss can be written as

$$\mathrm{PL} = \left(\left(\frac{\lambda}{4\pi}\right)^4 \cdot \left| \sum_{m=1}^{M} \sum_{n=1}^{N} \sum_{r=1}^{R} \sqrt{\frac{G_t(\varphi_m)G_e(\varphi_{mr})G_e(\varphi_{rn})G_r(\varphi_n)}{d_{mr}^2 d_{rn}^2}} \right|^2 \varepsilon_r \sigma_f \right)^{-1}. \tag{7}$$

3.3. PiBS Scenario. In this scenario, we set the phase of $\mathbf{b}_r$ to minimize the pathloss of the direction of S to the IRS and IRS to the D. $\mathbf{b}_r$ is related to $\tilde{\mathbf{d}}_{SR}$ and $\tilde{\mathbf{d}}_{RD}$, which is the unit vector of distances d_{SR} and d_{RD}. Therefore, $\mathbf{b}_r$ can be calculated by

$$\mathbf{b}_r = e^{-j(2\pi/\lambda)\left(\boldsymbol{\tau}_r \cdot \tilde{\mathbf{d}}_{SR} - \boldsymbol{\tau}_r \cdot \tilde{\mathbf{d}}_{RD}\right)}, \tag{8}$$

where $\boldsymbol{\tau}_r$ is the vector representing the position of the center of rth unit cell on the IRS pointing from the origin, as shown in Figure 3.

The pathloss model for the PiBS scenario can be obtained from formulas (3) and (8):

$$\mathrm{PL} = \left(\left(\frac{\lambda}{4\pi}\right)^4 \cdot \left| \sum_{m=1}^{M} \sum_{n=1}^{N} \sum_{r=1}^{R} \sqrt{\frac{G_t(\varphi_m)G_e(\varphi_{mr})G_e(\varphi_{rn})G_r(\varphi_n)}{d_{mr}^2 d_{rn}^2}} e^{j\zeta} \right|^2 \varepsilon_r \sigma_f \right)^{-1}, \tag{9}$$

where $\zeta = (2\pi/\lambda) \cdot (d_{mr} + \Delta d + d_{rn})$ and $\Delta d = \boldsymbol{\tau}_r \cdot (\mathbf{d}_{RD} - \mathbf{d}_{SR})$. ζ denotes the phase shift processing by the IRS, Δd denotes the total equivalent distance, and $(d_{mr} + \Delta d + d_{rn})$ denotes the equivalent distance on the IRS due to the different positions of the reflecting unit cells.

Although the pathloss obtained by the PiBS is not optimal, it has practical significance. In the real communication scenarios, it is easier to determine the orientation of the transceiver than the exact propagation distance.

4. Performance Analysis and Simulation Results

In this section, we analyze the performance of the proposed channel model through numerical results. The simulations
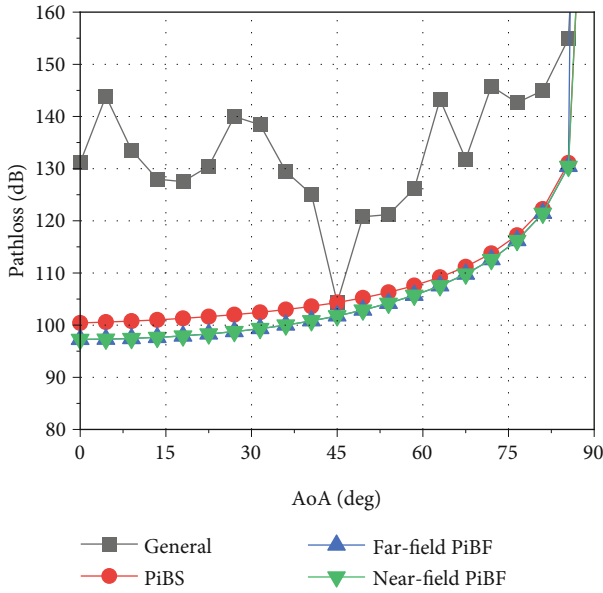
FIGURE 8: Pathloss relative to φ_{SR} for $\varphi_{RD} = 45°$.

of the pathloss are conducted based on the deformation expressions of the initial expression (3) in the general scenario (5), far-field PiBF (6), near-field PiBF (7), and PiBS scenario (9). In the numerical simulation, the considered system parameters are shown in Table 2.

It is assumed that the horizontal locations of the S, D, and IRS are fixed as the x-y plane. Figure 4(a) shows the pathloss variation with IRS size R when $d_{SR} = d_{RD} = 100$ m; it can be observed that both the PiBS and the PiBF successfully transmit the signal relative to the severe pathloss of the general scenario, and the pathloss is only related to the radiation pattern of the IRS units. According to the simulation results, the pathloss decreases as the number of units on the IRS increases in the PiBS and PiBF scenarios. However, in the general scenario, the pathloss shows a downward trend with great fluctuation. Figure 4(b) shows the pathloss variation with IRS size R when $d_{SR} = d_{RD} = 0.01$ m. Compared to Figure 4(a), the pathloss changes drastically in the PiBS scenario. In this case, the equivalent distance cannot substitute the actual distance. In addition, the near-field PiBF and far-field PiBF no longer coincide entirely when the distance is short, which is in agreement with our expected results.

Figure 5 shows the variation of the pathloss with the distance d_{SR} and d_{RD}. Simulation is based on setting $\varphi_{SR} = 60°$, $\varphi_{RD} = 30°$, and the size of the IRS $R = 1024$. In Figure 5(a), compared with the general scenario, the PiBF scenario has a significant improvement of about 34.9 dB, and for the PiBS is about 32 dB. As a result, although the impact of phase on the received power is reduced, it is not completely eliminated. In Figure 5(b), the simulation results are obtained near the threshold between the near and far field. Effective performance can still be obtained in this case, while Figure 5(c) shows the simulation results of the near-field case. According to the simulation result of the PiBS scenario, simply representing the actual distance by the equivalent

distance will result in an error in the calculation when the distance between the transceiver and IRS is close, similar to the size of the IRS. Therefore, an insightful conclusion can be obtained that when the far-field condition is met, the pathloss during transmission can be significantly reduced based on the orientation information. While in the near-field condition, information of the precise distance is essential.

The signal transmitted between different height of the S and D through the IRS in the four scenarios is shown in Figure 6. H_S is the vertical distance between the geometric center of S and the x-y plane. H_D is the vertical distance between the geometric center of D and the x-y plane. The sign of H_S and H_D is the same as the z-axis. Compared to the traditional situation, the pathloss decreases apparently and the fluctuation reduced efficiently in Figures 6(a)–6(d). The maximum loss in the PiBS, far-, and near-field PiBF scenarios are 63%, 59%, and 58% of the general scenario, respectively. We set the minimum value to 160 dB in Figure 6(a) for a more distinct comparison.

In Figure 7, the simulation is based on setting $d_{SR} = d_{RD} = 10$ m and the size of the IRS $R = 1024$. As shown in Figure 7(a), the pathloss is relatively low only when $\varphi_{SR} = \varphi_{RD}$ and depends on the angle in orientation dramatically. Figures 7(b)–7(d) show that after the phase shift of the unit cells on the IRS, the phase dependence and pathloss at the same AoA and AoD as the general scenario are reduced largely. Compared with Figures 7(c) and 7(d), Figure 7(b) reflects the asymmetric changes of AoA and AoD since the peculiarities of the phase processing of the PiBS scenario.

Figure 8 uses the same parameters as Figure 7 and depicts the snapshot at $\varphi_{RD} = 45°$. In Figure 8, the performance when the direction of the destination is unknown for the IRS is presented. For the general scenario, pathloss reaches the minimum only when $\varphi_{SR} = \varphi_{RD} = 45°$. However, for the PiBS and PiBF scenarios, there is a significant improvement on the robust of pathloss in the dimension of azimuth.

5. Conclusion

In this paper, the FSPL models in different scenarios for the IRS-assisted THz MIMO wireless communication system based on the physical and electromagnetic properties of the IRS are investigated. According to the initial form of pathloss, the FSPL of general scenario, far- and near-field PiBF scenarios, and PiBS scenario are proposed. Numerical results show that IRS can significantly reduce the pathloss during the propagation in THz band. Moreover, when the far-field condition is met, a similar effect of the PiBS and the PiBF scenario can be achieved. The results shown that the IRS-assisted channel propagation characteristics are related to the IRS size and the direction and distance of the transceivers. This model validates that the communication with IRS can be considered an effective technology to meet the demands of 6G wireless networks.

Appendix

The power received by the rth unit cell on the IRS that emitted by the mth antenna unit of S is

$$P_r^m = \frac{\lambda^2 P_m G_t(\varphi_m) G_e(\varphi_{mr})}{\left(4\pi d_{mr}^2\right)^2}, \tag{A.1}$$

where $P_m = P_t/M$. Assuming equal weights for each channel, we distribute the total transmit power equally.

The power reflected by the rth unit cell on the IRS and received by the nth antenna unit of D is

$$P_n^r = \frac{\lambda^2 P_r^s G_e(\varphi_{mr}) G_r(\varphi_n)}{\left(4\pi d_{rn}^2\right)^2}. \tag{A.2}$$

The efficiency factor ε_r is the ratio of the received power to the reflected power on the rth unit cell on the IRS and represents the insertion loss required to achieve phase change on the rth unit cell as well as the finite unit cell transmission efficiency. $\varepsilon_r < 1$ because the IRS is passive. σ_f is the atmospheric molecular absorption loss during THz wave transmission. The transmit power can be obtained by formulas (A.1) and (A.2):

$$P_{r,mn} = \left(\frac{\lambda}{4\pi}\right)^4 \frac{P_m G_t(\varphi_m) G_e(\varphi_{mr}) G_e(\varphi_{rn}) G_r(\varphi_n)}{d_{rn}^2 d_{mr}^2} \varepsilon_r \sigma_f. \tag{A.3}$$

The signal received by the receiving antenna at the destination is

$$y = \sum_{m=1}^{M} \sum_{n=1}^{N} \sum_{r=1}^{R} b_{r,mn} \sqrt{P_{r,mn}} e^{j\theta_{r,mn}}. \tag{A.4}$$

Substituting formulas (A.3) and (A.4) into the receiving power

$$P_R = \left| \sum_{m=1}^{M} \sum_{n=1}^{N} \sum_{r=1}^{R} b_{r,mn} \sqrt{P_{r,mn}} e^{j\theta_{r,mn}} \right|^2. \tag{A.5}$$

Formula (2) can be derived by the process above.

Data Availability

The data used to support the findings of this study is confidential.

Conflicts of Interest

The authors declare that they have no conflicts of interest.

Acknowledgments

References

[1] M. Z. Chowdhury, M. Shahjalal, S. Ahmed, and Y. M. Jang, "6G wireless communication systems: applications, requirements, technologies, challenges, and research directions," *IEEE Open Journal of the Communications Society*, vol. 1, pp. 957–975, 2020.

[2] M. A. ElMossallamy, H. Zhang, L. Song, K. G. Seddik, Z. Han, and G. Y. Li, "Reconfigurable intelligent surfaces for wireless communications: principles, challenges, and opportunities," *IEEE Transactions on Cognitive Communications and Networking*, vol. 6, no. 3, pp. 990–1002, 2020.

[3] Y. Liu, X. Liu, X. Mu et al., "Reconfigurable intelligent surfaces: principles and opportunities," *IEEE Communications Surveys & Tutorials*, vol. 23, no. 3, pp. 1546–1577, 2021.

[4] W. Fan, L. Hentilä, and P. Kyösti, "Spatial fading channel emulation for over-the-air testing of millimeter-wave radios: concepts and experimental validations," *Frontiers of Information Technology & Electronic Engineering*, vol. 22, no. 4, pp. 548–559, 2021.

[5] Y. Yuan, D. Wu, Y. Huang, and I. Chih-Lin, "Reconfigurable intelligent surface relay: lessons of the past and strategies for its success," *IEEE Communications Magazine*, vol. 60, no. 12, pp. 117–123, 2022.

[6] M. Di Renzo, A. Zappone, M. Debbah et al., "Smart radio environments empowered by reconfigurable intelligent surfaces: how it works, state of research, and the road ahead," *IEEE Journal on Selected Areas in Communications*, vol. 38, no. 11, pp. 2450–2525, 2020.

[7] R. Schroeder, J. He, G. Brante, and M. Juntti, "Two-stage channel estimation for hybrid RIS assisted MIMO systems," *IEEE Transactions on Communications*, vol. 70, no. 7, pp. 4793–4806, 2022.

[8] E. Basar and I. Yildirim, "Reconfigurable intelligent surfaces for future wireless networks: a channel modeling perspective," *IEEE Wireless Communications*, vol. 28, no. 3, pp. 108–114, 2021.

[9] J. Ye, S. Guo, and M.-S. Alouini, "Joint reflecting and precoding designs for SER minimization in reconfigurable intelligent surfaces assisted MIMO systems," *IEEE Transactions on Wireless Communications*, vol. 19, no. 8, pp. 5561–5574, 2020.

[10] K. Guan, G. Li, T. Kuerner et al., "On millimeter wave and THz mobile radio channel for smart rail mobility," *IEEE Transactions on Vehicular Technology*, vol. 66, no. 7, pp. 5658–5674, 2017.

[11] H. Jiang, B. Xiong, H. Zhang, and E. Basar, "Hybrids far- and near-field modeling for reconfigurable intelligent surface assisted V2V channels: a sub-array partition based approach," *IEEE Transactions on Wireless Communications*, p. 1, 2023.

[12] H. Gao, W. Wang, Y. Wu, Y. Liu, G. F. Pedersen, and W. Fan, "Experimental comparison of on–off and all-on calibration modes for beam-steering performance of mmWave phased array antenna-in-package," *IEEE Transactions on Instrumentation and Measurement*, vol. 70, pp. 1–9, 2021.

[13] E. Basar, M. Di Renzo, J. De Rosny, M. Debbah, M. Alouini, and R. Zhang, "Wireless communications through reconfigurable intelligent surfaces," *IEEE Access*, vol. 7, pp. 116753–116773, 2019.

[14] H. Jiang, B. Xiong, H. Zhang, and E. Basar, "Physics-based 3D end-to-end modeling for double-RIS assisted non-stationary UAV-to-ground communication channels," *IEEE Transactions on Communications*, vol. 71, no. 7, pp. 4247–4261, 2023.

[15] C. Huang, A. Zappone, G. C. Alexandropoulos, M. Debbah, and C. Yuen, "Reconfigurable intelligent surfaces for energy efficiency in wireless communication," *IEEE Transactions on Wireless Communications*, vol. 18, no. 8, pp. 4157–4170, 2019.

[16] E. Björnson, Ö. Özdogan, and E. G. Larsson, "Intelligent reflecting surface versus decode-and-forward: how large surfaces are needed to beat relaying?," *IEEE Wireless Communications Letters*, vol. 9, no. 2, pp. 244–248, 2020.

[17] Z. Abdullah, S. Kisseleff, K. Ntontin, W. A. Martins, S. Chatzinotas, and B. Ottersten, "Double-RIS communication with DF relaying for coverage extension: is one relay enough?," in *ICC 2022-IEEE International Conference on Communications*, pp. 2639–2644, Seoul, Korea, Aug. 2022.

[18] M. Nemati, J. Park, and J. Choi, "RIS-assisted coverage enhancement in millimeter-wave cellular networks," *IEEE Access*, vol. 8, pp. 188171–188185, 2020.

[19] W. Tang, M. Z. Chen, X. Chen et al., "Wireless communications with reconfigurable intelligent surface: path loss modeling and experimental measurement," *IEEE Transactions on Wireless Communications*, vol. 20, no. 1, pp. 421–439, 2021.

[20] J. Kokkoniemi, J. Lehtomäki, and M. Juntti, "A line-of-sight channel model for the 100–450 gigahertz frequency band," *EURASIP Journal on Wireless Communications and Networking*, vol. 2021, 15 pages, 2021.

[21] W. L. Stutzman and G. A. Thiele, *Antenna Theory Design, 3rd Ed*, Wiley, New York, NY, USA, 2012.